

Discovery of Extended X-Ray emission from the unidentified TeV source HESS J1614–518 using the Suzaku Satellite

Hironori MATSUMOTO¹, Hideki UCHIYAMA¹, Makoto SAWADA¹,
Takeshi G. TSURU¹, Katsuji KOYAMA¹, Hideaki KATAGIRI²,
Ryo YAMAZAKI², Aya BAMBA³, Kazunori KOHRI⁴, Koji MORI⁵,
and

Yasunobu UCHIYAMA³

¹*Department of Physics, Graduate School of Science, Kyoto University, Sakyo-ku, Kyoto 606-8502*

E-mail (HM) matumoto@cr.scphys.kyoto-u.ac.jp

²*Department of Physical Science, Hiroshima University, Higashi-Hiroshima 739-8526*

³*Institute of Space and Astronautical Science, Japan Aerospace Exploration Agency,
3-1-1 Yoshinodai, Sagami-hara, Kanagawa 229-8510*

⁴*Physics Department, Lancaster University LA1 4YB, UK*

⁵*Department of Applied Physics, University of Miyazaki,
1-1 Gakuen Kibana-dai Nishi, Miyazaki 889-2192*

(Received 2007 June 18; accepted 2007 November 1)

Abstract

We report the Suzaku results of HESS J1614–518, which is the brightest extended TeV gamma-ray source discovered in the Galactic plane survey conducted using the H.E.S.S. telescope. We discovered three X-ray objects in the field of view of the X-ray Imaging Spectrometer (XIS), which were designated as Suzaku J1614–5141 (src A), Suzaku J1614–5152 (src B), and Suzaku J1614–5148 (src C). Src A is an extended source located at the peak position of HESS J1614–518, and therefore it is a plausible counterpart to HESS J1614–518. The X-ray flux in the 2–10 keV band is $5 \times 10^{-13} \text{ erg s}^{-1} \text{ cm}^{-2}$, which is an order of magnitude smaller than the TeV flux. The photon index is 1.7, which is smaller than the canonical value of synchrotron emissions from high-energy electrons found in some supernova remnants. These findings present a challenge to models in which the origin of the TeV emission is the inverse Compton scattering of the cosmic microwave background by accelerated electrons that emit X-rays via synchrotron emission. Src B is located at a relatively dim region in the TeV band image; however, its hydrogen column density is the same as that of src A. Therefore, src B may also be physically related to HESS J1614–518. Src C is a foreground late-type B star. We also discovered a soft extended X-ray emission near HESS J1614–518.

Key words: acceleration of particles—X-rays: individual (HESS J1614–518)—ISM: cosmic rays

1. Introduction

One of the striking results of the TeV γ -ray astronomy with the H.E.S.S. Cerenkov Telescope is the discovery of many very high-energy (VHE) objects along the Galactic plane (Aharonian et al. 2005a; Aharonian et al. 2006). Most of these objects are spatially extended to $\gtrsim 0.1^\circ$, and could therefore be Galactic objects, such as supernova remnants (SNR) or pulsar wind nebulae (PWN). TeV γ -ray emissions are also detected from a young stellar cloud, Westerlund 2 (Aharonian et al. 2007). These provide direct evidence that the inner Galactic region produces high-energy particles with energies above TeV level. Observations of other wavelengths, particularly X-rays, provide a better understanding of which particles are accelerated and the relevant dynamics. High-energy electrons predominantly emit synchrotron X-rays in a typical interstellar magnetic field with strength of a few micro-Gauss. Therefore, the flux ratio of the X-rays to TeV γ -rays provides valuable information that can distinguish whether the accelerated particles are protons or electrons.

At present, however, X-ray observations on these TeV sources are still limited. Matsumoto et al. (2007) observed HESS J1616–508 deeply with the Suzaku satellite (Mitsuda et al. 2007), in addition to analyzing the archival data obtained from XMM-Newton. However, they found no X-ray counterpart with a severe upper limit of $3 \times 10^{-13} \text{ erg s}^{-1} \text{ cm}^{-2}$ in the 2–10 keV band (see also Landi et al. 2007). HESS J1303–631 (Aharonian et al. 2005b) is the same example. On the other hand, HESS J1804–216 has some X-ray counterparts (Landi et al. 2006; Cui & Konopelko 2006; Bamba et al. 2007; Kargaltsev et al. 2007a); however, their physical connection to HESS J1804–216 is still unclear. Recently, an extended X-ray emission from TeV J2032+4130 (Aharonian et al. 2002) that has a peak position coincident with that of the γ -ray emission was discovered as a result of a deep observation with XMM-Newton (Horns et al. 2007). However, Butt (2007) was skeptical about the detection of the diffuse emission, and argued that it can be explained by integrated emission of faint X-ray sources detected with Chandra (Butt et al. 2006). Recently, an

extended X-ray emission from HESS J1834–087 was discovered with XMM-Newton (Tian et al. 2007), which is a clear identification. However, there are also point-like sources in addition to the extended emission in the spectral region reported by Tian et al. (2007); therefore, the physical connection between the extended emission and HESS J1834–087 remains unclear. Absolutely, it is imperative to have an access to more X-ray samples with a physical connection to the VHE objects. Therefore, we observed HESS J1614–518 (hereafter HESS J1614) with the Suzaku satellite, which is the brightest among the newly discovered HESS objects (Aharonian et al. 2005a; Aharonian et al. 2006). Two X-ray objects were found in the vicinity of HESS J1614 using the Swift/X-Ray Telescope (XRT) (Landi et al. 2006). However, neither of them coincided with the γ -ray peak of HESS J1614; therefore their physical connection to HESS J1614 could not be clarified. Since HESS J1614 has a spatial extension of $\sim 10'$, high-sensitivity observations in a hard X-ray band with low and stable backgrounds are essential. The Suzaku X-ray Imaging Spectrometer (XIS; Koyama et al. 2007), combined with the X-Ray Telescope (XRT; Serlemitsos et al. 2007), satisfies these requirements and is regarded as one of the best instruments to search for diffuse X-ray emissions, particularly in the hard-energy band. Uncertainties quoted in this study are at the 90% confidence level, and errors on the data points in the X-ray spectra and radial profiles are at the 1σ confidence level, unless otherwise stated.

2. Observations and Data Reduction

The brightest part of HESS J1614 was observed on 2006 September 16. The on-source observation was followed by a background observation at an offset position (figure 1), where no known bright X-ray or γ -ray source existed in the field of view. The latitude of the offset position is selected to be almost the same as the position of HESS J1614, so that the Galactic ridge emission at the source position can be reliably subtracted (e.g., Worrall et al. 1982; Warwick et al. 1985; Koyama et al. 1986; Yamauchi, Koyama 1993; Kaneda et al. 1997; Ebisawa et al. 2001; Ebisawa et al. 2005; Sugizaki et al. 2001; Tanaka 2002; Revnivtsev et al. 2006). The observations are summarized in table 1.

The observations were performed with the four CCD cameras (XIS) located at the focal planes of four XRTs. One of the XIS sensors (XIS1) has a back-illuminated (BI) CCD, while the other three sensors (XIS0, 2, and 3) utilize front-illuminated (FI) CCDs. The XIS was operated in the normal clocking mode with no charge injection technique. Although the non-imaging Hard X-ray Detector (HXD; Kokubun et al. 2007; Takahashi et al. 2007) was also available, in this study, we focus on the XIS data analysis because our main objective is searching for X-ray counterparts of HESS J1614 using the imaging capability.

Data were reduced and analyzed using the processed data of version 1.2.2.3¹, the HEADAS software version

6.2, and a calibration database (CALDB) released on 2007 April 9. All data affected by the South Atlantic Anomaly and/or telemetry saturation were excluded. We also excluded the data obtained with low elevation angles from the Earth rim that were below $< 5^\circ$ ². Finally, we removed the hot and flickering pixels. After these data screenings, the effective exposures were 44.5 ks and 53.1 ks on the HESS J1614 and the offset background, respectively.

We checked the energy scale of each XIS sensor using the calibration source (^{55}Fe) and confirmed that the observed center energies of $K\alpha$ and $K\beta$ lines were in good agreement with the expected values (5.895 and 6.490 keV) within the nominal calibration uncertainty of 0.2% (Koyama et al. 2007).

3. Analysis and Results

3.1. XIS image

We extracted XIS images from each sensor using the screened data for the soft- and hard-energy bands. For the FI sensors, the soft- and hard-bands are defined as 0.4–3.0 keV and 3.0–10.0 keV, respectively, while those for the BI sensor are defined as 0.3–3.0 and 3.0–7.0 keV, respectively. We excluded the corners of the CCD chips illuminated by the ^{55}Fe calibration sources. Images of the non-X-ray background (NXB) were obtained from the night Earth data provided by the XIS team (Tawa et al. 2007) and subtracted from the HESS J1614 images. Then, the soft and hard images were divided by flat sky images simulated at 1.49 and 6.0 keV using the XRT+XIS simulator *xissim* (Ishisaki et al. 2007) for vignetting corrections. The images from the three FI sensors were summed and re-binned by a factor of 8.

The XIS FI images of the HESS J1614 region shown in figure 2 were smoothed using a Gaussian function with a sigma of $0'.28$. The BI images were essentially the same except for the poorer statistics. In the hard-band image, an extended object with a peak position of $(l, b) = (331^\circ 64, -0^\circ 51)$ ³ was found, and was designated as Suzaku J1614–5141 (src A). The position uncertainty was $0'.8$. Src A was not conspicuous in the soft-band image. Another bright X-ray object, found at $(l, b) = (331^\circ 45, -0^\circ 60)$ ⁴, was also bright in the soft X-ray band. The position uncertainty was $0'.8$. We designated this object as Suzaku J1614–5152 (src B). In the soft-band image, an X-ray source was found at $(l, b) = (331^\circ 58, -0^\circ 62)$

² We did not screen the data with the elevation angles from the bright Earth rim in order to maximize the statistics, although the standard data processing done at ISAS/JAXA or NASA/GSFC usually use this screening. The bright Earth may contaminate the soft-band spectra. In our case, however, we confirmed that the standard screening reduced the effective exposures but did not affect the XIS spectra. For example, excluding the data with low elevation angles from the bright Earth rim of $< 20^\circ$ changed the counting rate of XIS1 in the 0.2–2 keV band from $0.1722 \text{ cts s}^{-1}$ to $0.1726 \text{ cts s}^{-1}$, while the exposure time decreased from 44.5ks to 40.3ks.

³ $(\alpha, \delta)_{\text{J2000.0}} = (16^{\text{h}} 14^{\text{m}} 34^{\text{s}}, -51^\circ 41' 00'')$

⁴ $(\alpha, \delta)_{\text{J2000.0}} = (16^{\text{h}} 14^{\text{m}} 06^{\text{s}}, -51^\circ 52' 38'')$

¹ See <http://www.astro.isas.jaxa.jp/suzaku/process/history/v1223.html>

Table 1. Log of Suzaku observations.

Name	OBSID	Pointing direction		Observation start (UT)	Effective exposure (ks)
		l	b		
HESS J1614	501042010	331°5717	−0°5274	2006/09/15 16:00	44.5
offset	501043010	330°3961	−0°3760	2006/09/16 11:02	53.1

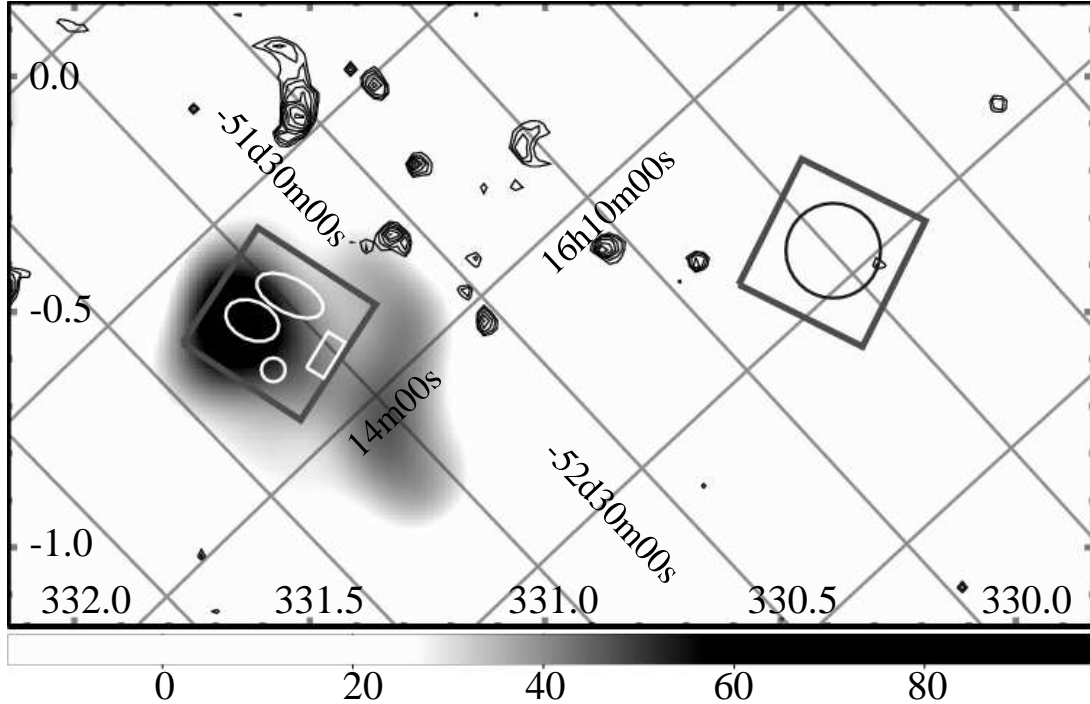


Fig. 1. Suzaku fields of view (thick boxes) overlaid on the H.E.S.S. smoothed excess map (same as figure 9 in Aharonian et al. 2006). The scale bar below the figure represents the excess. The coordinates on the exterior frame are Galactic, while the grid shows the equatorial coordinates (J2000.0). The contour lines denote the radio emission (843 MHz) adopted from the Sydney University Molonglo Sky Survey (SUMSS; Bock et al. 1999). The contours are drawn from 0.1 Jy beam^{-1} on a logarithmic scale with a factor of 0.158, where the FWHM beam size is $\sim 0'.7 \times 0'.9$. Regions outlined by thin solid lines are the ones used in our spectral analyses (see section 3).

⁵ and was designated as Suzaku J1614–5148 (src C). The position uncertainty was $0'.6$.

We obtained the radial profiles and compared with a point-spread function (PSF). As for the PSF, we obtained the radial profiles using the SS Cyg data observed on 2005 November 2 (OBSID=400006010), which is the verification phase data for the imaging capability of the XRT (Serlemitsos et al. 2007). Since the energy dependence of the PSF is almost negligible (Serlemitsos et al. 2007), it was extracted from the 0.4–10 keV band. Figure 3 shows the radial profile of src A in the hard-energy band. The profile cannot be fitted with the PSF plus a constant component model ($\chi^2/\text{d.o.f.} = 45.7/13$), and therefore src A should be an extended source. Since src B is located near the edge of the XIS field of view, and therefore the PSF is largely distorted, it is impossible to study the radial profile of src B in detail. However, the hard-band image suggested that src B is extended. The radial profile of src C is consistent with the PSF plus a

constant component ($\chi^2/\text{d.o.f.} = 37.1/26$), supporting the assumption of a point source.

3.2. XIS spectrum

3.2.1. Background spectra: blank and offset positions

Since the source position is on the Galactic ridge, the local Galactic emission (the ridge emission), as well as the NXB and cosmic X-ray background, cannot be ignored. To account for the background, we compared the spectrum from the blank region near the sources (see the solid line in figure 2) with that from the offset position. The spectra of the offset position correspond to a circular region of $6'$ radius at the center of the field of view.

For the most accurate NXB estimation, we sorted the night Earth data so that the cut-off rigidity distribution was the same as that of the HESS J1614 and offset observations. Since the NXB depends on a location on the detector (Yamaguchi et al. 2006), we extracted the NXB spectra from the same regions used to determine the blank and offset regions in detector coordinates (DETX/Y). The

⁵ $(\alpha, \delta)_{\text{J2000.0}} = (16^{\text{h}}14^{\text{m}}47^{\text{s}}, -51^{\circ}48'36'')$

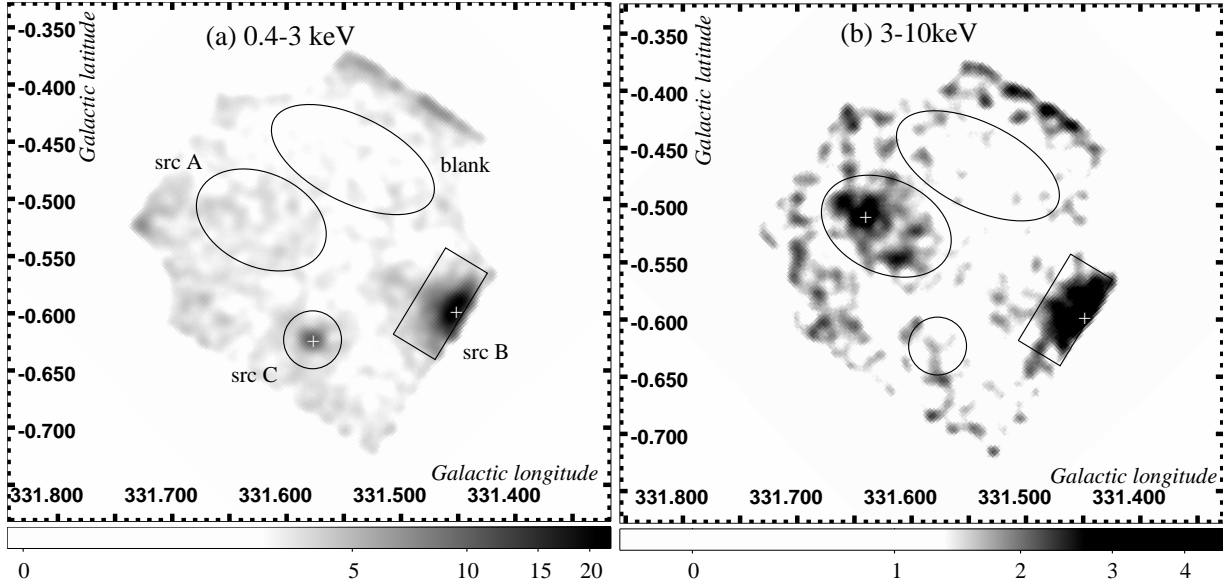


Fig. 2. Suzaku XIS FI (XIS0+2+3) images of the HESS J1614 region in the Galactic coordinates: (a) 0.4–3 keV and (b) 3–10 keV band. The images were smoothed using a Gaussian function with a sigma of 0'28. Vignetting correction was applied after subtracting NXB as described in the text. Regions represented with solid lines are used in our spectral analyses (see section 3.2). Plus marks represent the peak position of each source.

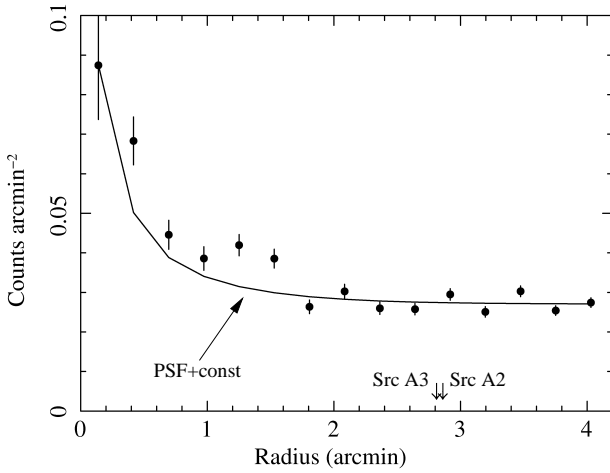


Fig. 3. Radial profile of src A extracted from the hard-band image of the XIS FI sensor (XIS0+2+3). The solid line represents the XIS PSF profile with a constant component. The downward arrows represent the positions of src A2 and A3 defined in section 3.2.3 (see figure 7).

NXB spectra thus obtained were then subtracted, and the resulting spectra of the blank and offset regions are shown in figure 4. The offset spectra were normalized to the same area as that of the blank region. We can clearly observe that the spectra of the blank region show an enhancement less than 3.0 keV.

The excess spectra of the blank region after subtracting the data of the offset position are shown in figure 5. We fitted these spectra with an absorbed power-law model, and the cross sections of photoelectric absorption were obtained from Morrison & McCammon (1983). We ob-

tained detector responses (RMF) and telescope responses (ARF) using both the `xismfgen` and `xissimarfgen` software (Ishisaki et al. 2007). In this case, a hydrogen-equivalent column density (N_H), a photon index (Γ), and normalization are free parameters. The best-fit parameters are summarized in table 2. Although the data were fitted acceptably with the power-law model, we can see some indications of emission lines in the residual, particularly at ~ 1.3 keV. When we added a Gaussian line model with $\sigma = 0$ (i.e., the delta function) to the power-law model, the peak energy became $1.33^{+0.04}_{-0.04}$ keV and the equivalent width was 24.0 (<53.1) eV, although the F-test does not require the use of a Gaussian model. These results suggest the emission line of MgXI and a thermal spectrum. Therefore we tried to fit the spectra with a thin-thermal plasma model (the APEC model; Smith et al. 2001), where the solar abundance of elements is obtained from Anders, Grevesse (1989). The free parameters are plasma temperature (kT), metal abundance, N_H , and normalization. The spectra were fitted acceptably with the plasma model, as summarized in table 2. However, the metal abundance is almost zero.

Since the blank region is in a dim area of both the soft- and hard-energy bands (figure 2), the soft excess must also exist in the regions of src A, B, and C. As for the source spectra, we concern the excess flux over this soft excess emission, and therefore used the blank region as background in the following analyses of the source spectra.

3.2.2. Extraction of the source spectra

We represented the source regions of src A, B, and C as solid lines in figure 2. We extracted light curves corresponding to the sources in the soft- and hard-energy bands from these regions and observed that none of them exhib-

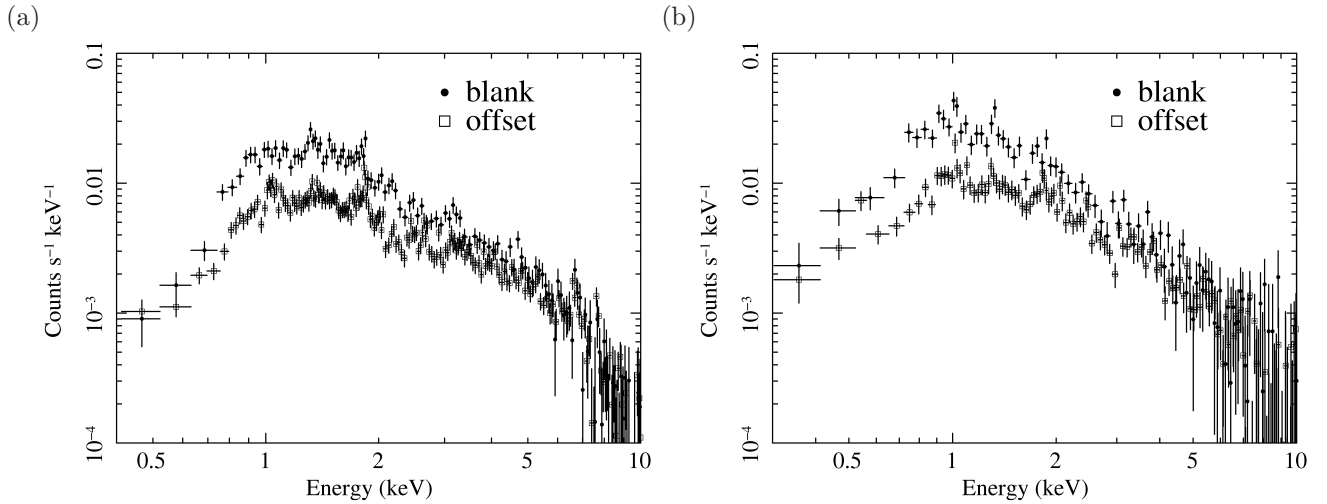


Fig. 4. XIS spectra of the blank and offset regions: (a) FI spectra (XIS0+2+3) and (b) BI (XIS1) spectra. The offset spectra were normalized to the same area as that of the blank region. The NXBs were subtracted as described in the text.

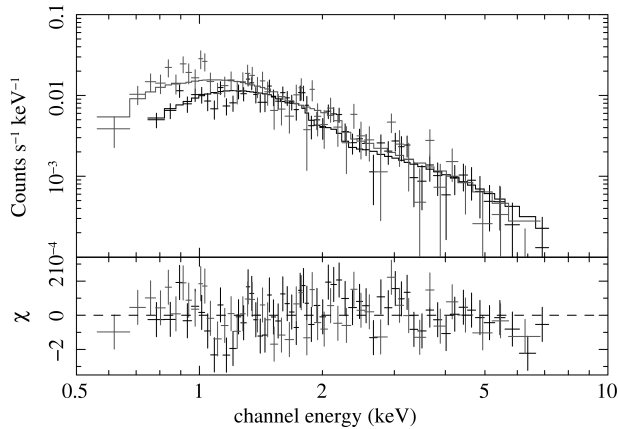


Fig. 5. Spectra of the blank region and the best-fit power-law model. The spectra of the offset region are subtracted as background. Black and gray lines represent the data and model for the XIS FI (XIS0+2+3) and BI (XIS1), respectively.

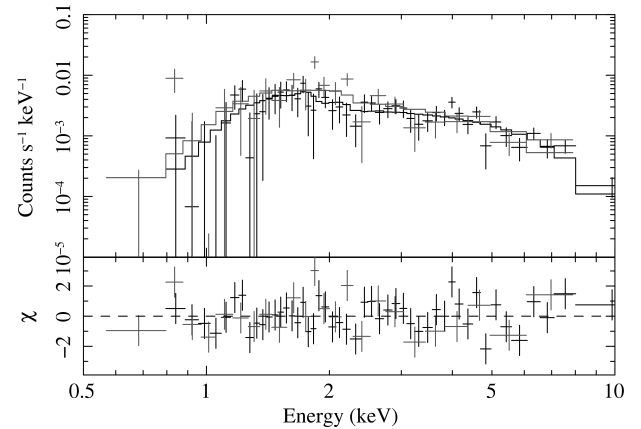


Fig. 6. XIS spectra of src A and the best-fit power-law model. Black and gray lines represent the data and the model for the XIS FI (XIS0+2+3) and BI (XIS1), respectively.

ited clear time variability. We extracted the XIS spectra of src A, B, and C by subtracting the NXB spectra, in the same manner as in the previous section. We then combined the NXB subtracted spectra obtained from three FI sensors.

3.2.3. Src A

The spectra of src A are shown in figure 6. Although the statistics are limited, no clear emission line was observed. We therefore fitted the spectra with the absorbed power-law model and obtained acceptable results. The best-fit parameters are summarized in table 2. In addition, we also tried to fit the spectra with the thermal plasma model. The best-fit parameters were $N_H = 1.04^{+0.34}_{-0.36} \times 10^{22} \text{ cm}^{-2}$, $kT = 10.0^{+26.0}_{-4.2} \text{ keV}$, and an abundance of $0.18 (< 0.93)$ solar with $\chi^2/\text{d.o.f.} = 80.01/67$. From a statistical viewpoint, neither of the models is rejected at a confidence level of 90 %. However, the thermal plasma model yields an uncomfortably high temperature

and an extremely low abundance, and therefore is not practicable. We therefore adopted the power-law model in all subsequent analyses and discussions.

Figure 7(a) is a close-up view of src A in the XIS FI hard-band image (figure 2). One could argue that src A is not a single extended source, but instead consists of multiple objects. To verify this possibility, we defined three circular regions designated as A1, A2, and A3 in the figure, and extracted the corresponding spectra. The radii of the source regions are $2'$, $1'$, and $1'$ for A1, A2, and A3, respectively. However, the statistics are poor and with the exception of the corresponding normalizations, no clear difference between these sources was observed (figure 7(b)). The spectra are described by a power-law model with a best-fit $\chi^2/\text{d.o.f.}$ of 25.72/31, 13.35/23, and 23.03/23, for A1, A2, and A3, respectively. The observed fluxes in the 0.5–10.0 keV band are $2.9 \times 10^{-13} \text{ erg s}^{-1} \text{ cm}^{-2}$, $1.1 \times 10^{-13} \text{ erg s}^{-1} \text{ cm}^{-2}$, and $0.95 \times 10^{-13} \text{ erg s}^{-1} \text{ cm}^{-2}$, for A1, A2, and A3, respec-

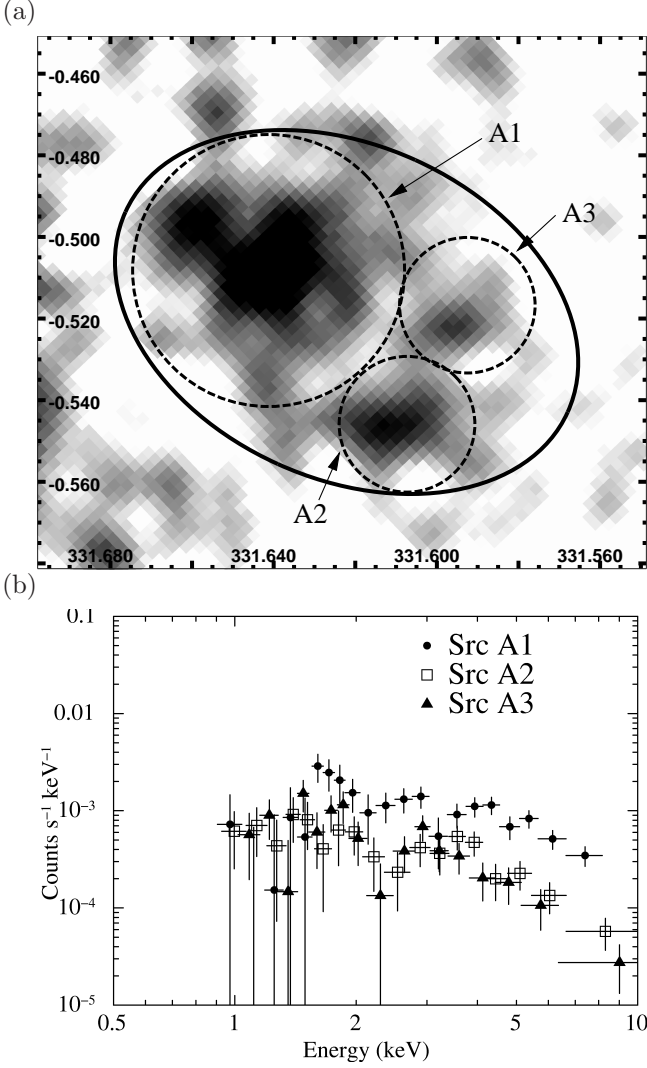


Fig. 7. (a) Close-up view of src A in the XIS FI hard-band image (figure 2). A large ellipse shows the spectral region for src A. Dotted circles designated as A1, A2, and A3 are the regions we studied to check for spatial variation of the spectra in src A. (b) Spectra extracted from regions A1, A2, and A3, as shown in figure 7(a). For clarity, only the spectra obtained by the FI sensors (XIS0+2+3) are shown.

tively. The best-fit parameters are summarized as follows: $N_H = 1.40^{+0.86}_{-0.67} \times 10^{22} \text{ cm}^{-2}$ and $\Gamma = 1.41^{+0.46}_{-0.42}$ for the A1 region, $N_H = 0.66^{+0.91}_{-0.57} \times 10^{22} \text{ cm}^{-2}$ and $\Gamma = 1.39^{+0.57}_{-0.49}$ for the A2 region, and $N_H = 1.47^{+0.99}_{-0.70} \times 10^{22} \text{ cm}^{-2}$ and $\Gamma = 2.26^{+0.72}_{-0.58}$ for the A3 region. All these parameters are consistent with the best-fit values of src A presented in table 2, which supports the hypothesis that src A1, A2, and A3 are substructures of src A.

3.2.4. Src B

The spectra of src B are shown in figure 8. We fitted the power-law model with the best-fit parameters as listed in table 2. Although no emission line was observed in the spectra, we also tried fitting a thermal plasma model. The best-fit χ^2 value of 196.13 for 159 degrees of freedom rejected the validity of a thermal plasma

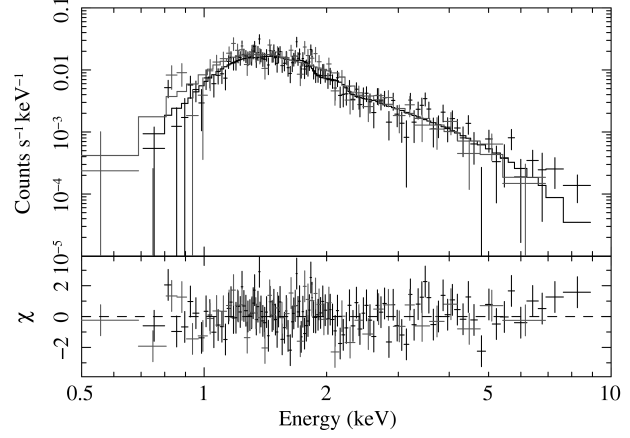


Fig. 8. XIS spectra of src B, shown with the best-fit power-law model. Black and gray lines represent the data and the model for the XIS FI (XIS0+2+3) and BI (XIS1), respectively

model at a confidence level of 97%. Nevertheless, for the sake of comparison, following are the best-fit parameters: $N_H = 0.84^{+0.09}_{-0.11} \times 10^{22} \text{ cm}^{-2}$, $kT = 1.28^{+0.21}_{-0.13} \text{ keV}$, and a metal abundance of zero (< 0.019) solar.

Src B is at the edge of the field of view. According to a simulation performed using *xissim*, the probability of detecting incident photons reduces by a factor of ~ 0.7 because some photons fall outside of the field of view. Furthermore, considering the fluctuation of the pointing direction due to the variation of the relative alignment between the XRT and the Attitude and Orbit Controlling System (AOCS; Serlemitsos et al. 2007), even more photons can escape from the field of view. Consequently, all the obtained parameters, particularly flux, could have large systematic errors.

3.2.5. Src C

We found that the spectra of src C can be fitted with the thermal plasma model, as shown in figure 9. The best-fit parameters are listed in table 2. Although the spectra can also be fitted with a power-law model having best-fit values as $N_H = 1.01^{+0.53}_{-0.36} \times 10^{22} \text{ cm}^{-2}$, and $\Gamma = 8.63^{+3.29}_{-2.25}$ with $\chi^2/\text{d.o.f.} = 63.76/52$, the obtained photon index is unreasonably large. Therefore, the thermal plasma model seems more suitable for practical use.

4. Discussion

4.1. Src A

Src A is the closest source to the peak position of HESS J1614, and both the X-ray and TeV γ -ray emissions are extended. Therefore, src A is a plausible X-ray counterpart to HESS J1614. The X-ray spectrum is described using the power-law model with $\Gamma = 1.73$, and the absorption-corrected flux in the 2–10 keV band is $5.3 \times 10^{-13} \text{ erg s}^{-1} \text{ cm}^{-2}$, while the γ -ray spectrum yields $\Gamma = 2.46$ and the flux in the 1–10 TeV band from a circular region of 0.4° is estimated to be $1.8 \times 10^{-11} \text{ erg s}^{-1} \text{ cm}^{-2}$ (Aharonian et al. 2006).

Table 2. Best-fit results of the XIS spectra.

	blank		src A	src B	src C
BGD [†]	offset	offset	blank	blank	blank
Model [‡]	PL	APEC	PL	PL	APEC
N_{H} (10^{22}cm^{-2})	$0.24^{+0.08}_{-0.07}$	$0.10^{+0.05}_{-0.04}$	$1.21^{+0.50}_{-0.41}$	$1.24^{+0.14}_{-0.13}$	$0.28^{+0.19}_{-0.19}$
Γ/kT (keV)	$2.38^{+0.19}_{-0.17}$	$2.72^{+0.50}_{-0.43}$	$1.73^{+0.33}_{-0.30}$	$3.60^{+0.24}_{-0.22}$	$0.63^{+0.15}_{-0.06}$
Abundance (solar)	—	$0.00(<0.029)$	—	—	$0.18^{+1.10}_{-0.10}$
$F_{0.5-10\text{keV}}^{\text{obs}} \P$	0.10	0.096	5.4	5.1	0.86
$F_{0.5-10\text{keV}}^{\text{abscor}} \S$	0.15	0.11	8.4	35.8	2.0
$F_{2-10\text{keV}}^{\text{obs}} \P$	0.058	0.050	4.8	3.0	0.071
$F_{2-10\text{keV}}^{\text{abscor}} \S$	0.059	0.051	5.3	3.6	0.076
$\chi^2/\text{d.o.f.}$	121.45/103	111.37/102	78.38/68	172.65/160	42.45/51

[†] Background spectrum used for the analysis.

[‡] Model used for the spectrum fitting: “PL” is a power-law model, and “APEC” is a thin thermal plasma model.

[¶] Observed flux in the 0.5–10 keV or 2–10 keV band in the unit of 10^{-13} erg s $^{-1}$ cm $^{-2}$. For the blank region, values are normalized to a region of 1 arcmin 2 (i.e., erg s $^{-1}$ cm $^{-2}$ arcmin $^{-2}$).

[§] Absorption corrected flux in the 0.5–10 keV or 2–10 keV band in the unit of 10^{-13} erg s $^{-1}$ cm $^{-2}$. For the blank region, values are normalized to a region of 1 arcmin 2 (i.e., erg s $^{-1}$ cm $^{-2}$ arcmin $^{-2}$).

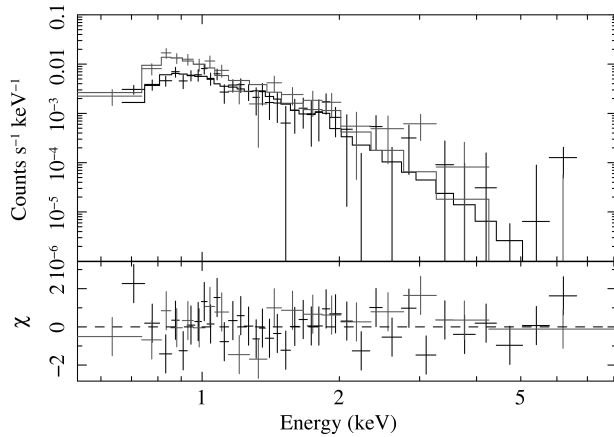


Fig. 9. XIS spectra of src C, shown with the best-fit thermal plasma model. Black and gray lines represent the data and the model for the XIS FI (XIS0+2+3) and BI (XIS1), respectively

Therefore, the flux ratio $F(1-10\text{ TeV})/F(2-10\text{ keV})$ is ~ 34 , which is one of the largest values observed among extended VHE objects (see Matsumoto et al. 2007 and references therein).

We first examined the difference between the peak positions of src A and HESS J1614. Since the peak position of TeV γ -ray is not presented in the study by Aharonian et al. (2006), we only worked in the bright region of figure 1 and fitted it with a Gaussian function. The peak position thus estimated is $(l, b) = (331^\circ 65', -0^\circ 52')^6$, which is ~ 0.8 away from the X-ray peak of src A. Considering that the best H.E.S.S. angular resolution is $\sim 5'$ (Aharonian et al. 2006), and from the position uncertainty of src A ($\sim 0.8'$), we can conclude that src A spatially coincides with the

peak of HESS J1614.

If src A is physically associated with HESS J1614, the best-fit column density (1.2×10^{22} cm $^{-2}$) suggests that the distance to HESS J1614 is roughly ~ 10 kpc, since the best-fit value is approximately equal to half of the total Galactic HI column density towards the HESS J1614 region ($\sim 2.2 \times 10^{22}$ cm $^{-2}$; Dickey & Lockman 1990). Assuming a distance of 10 kpc, the luminosity of src A in the 2–10 keV band is 6×10^{33} erg s $^{-1}$.

This region was also observed with the Swift XRT (Landi et al. 2006); however, no source was found at the position of src A. This is probably due to the limited exposure time (~ 1700 s), and/or the small effective area of the Swift XRT. Furthermore, src A is near the edge of the field of view of the Swift XRT, which makes the detection more difficult. No counterparts in the other wavelengths are found in literatures.

If the origin of the TeV emission is the inverse Compton scattering of the cosmic microwave background by high-energy electrons of a single population, the large flux ratio $F(1-10\text{ TeV})/F(2-10\text{ keV}) \sim 34$ requires a low magnetic field. The spectral energy distribution (SED) of src A and HESS J1614 are plotted in figure 10. In the same figure, we also plotted the estimated synchrotron flux of the high-energy electrons in the magnetic fields with intensities $B = 0.1, 1, \text{ and } 10 \mu\text{Gauss}$. The low X-ray flux of src A requires a magnetic field of $B \lesssim 1 \mu\text{G}$, which is smaller than the typical interstellar magnetic field intensity of a few micro-Gauss. This is similar to what is observed in HESS J1616–508 (Matsumoto et al. 2007); however, but in that case, a possibility of a magnetic field of a few micro-Gauss and a strong cut-off in the electron energy distribution greater than $\sim 10^{14}$ eV cannot be excluded. However, Src A has a small spectral index, which does not favor this possibility.

On the other hand, interstellar radiations whose wave-

⁶ $(\alpha, \delta)_{\text{J2000.0}} = (16^{\text{h}}14^{\text{m}}41^{\text{s}}, -51^\circ 41' 03'')$

lengths are shorter than those of the CMB (e.g., far-infrared) also have large energy density (Moskalenko et al. 2006). If the seeds of the inverse Compton are such photons, the electrons produce synchrotron emission at wavelengths longer than X-rays in regions with a magnetic field of a few micro-Gauss, and therefore our Suzaku results would have no constraints on the magnetic field intensity.

Since src A is extended, it may be an SNR. However, the observed X-rays are probably not due to ordinary synchrotron emission, because the photon index (~ 1.7) is smaller than the typical values of non-thermal SNRs such as SN1006 (~ 2.5 – 3.0 ; Bamba et al. 2005). The X-ray spectrum of the SNR γ Cygni also has a small photon index of 0.8 – 1.5 (Uchiyama et al. 2002), which can be considered as a non-thermal bremsstrahlung from accelerated electrons; the energy distribution of the accelerated electrons below the Coulomb break is flattened due to the Coulomb interactions with ambient molecular clouds (Uchiyama et al. 2002). In that scenario, a photon index less than 1.5 is expected for viable acceleration mechanisms. Since the photon index of src A is marginally consistent with this criterion, the observations of src A could be explained with this scenario. In addition, undetected molecular clouds responsible for the bremsstrahlung may exist. Yamazaki et al. (2006) suggested that the TeV-to-X-ray flux ratio of old SNRs with an age of $\sim 10^5$ years can be very large, in some cases more than 100. The small photon index of src A may support this scenario, where X-ray emission is dominated by synchrotron emission from secondary electrons that may have a smaller index than that of the primary electrons. However, no radio counterpart has been observed in the HESS J1614 region, which could pose a severe problem for the SNR scenarios. For example, there is no enhancement in the 843 MHz band (figure 1), where the rms noise level is ~ 2 mJy arcmin $^{-2}$ (Bock et al. 1999).

Massive stars can be the origin of the extended TeV γ -ray emission; Torres & Domingo-Santamaría (2007) proposed that stellar winds can produce hadronic γ -rays by interacting with cosmic rays. Anchordoqui et al. (2007) argue that TeV γ -rays are the result of Lorentz-boosted MeV γ -rays, which are emitted due to the de-excitation of daughter nuclei resulting from collisions between high-energy nuclei (the cosmic rays) and UV photons from the massive stars. In either case, X-rays may originate from stellar winds from the OB stars. These models have been proposed in order to explain the origin of the unidentified TeV source, TeV J2032+4130. Although the X-ray photon index of TeV J2032+4130 is similar to that of src A, the flux ratio $F(1-10 \text{ TeV})/F(2-10 \text{ keV})$ (~ 2 – 3) is much smaller than that of src A (Horns et al. 2007). Furthermore, no OB stars have been observed around HESS1614.

Another possibility is a PWN; some PWNe have a small photon index (Fleishman & Bietenholz 2007 and references therein). The luminosity, assuming the distance of 10 kpc, is not unusual for X-ray PWNe (Cheng et al. 2004). A pulsar driving the nebula may be hidden in the middle of src A, or src B itself could be the pul-

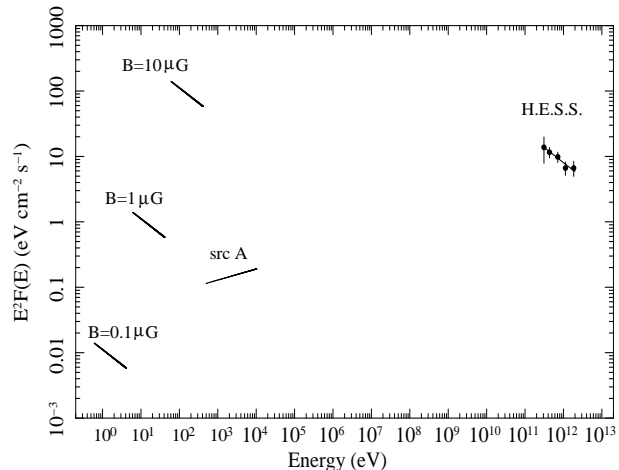


Fig. 10. Spectral energy distribution of src A and HESS J1614 from the X-ray to TeV γ -ray bands. The synchrotron radiation from accelerated electrons, which kick the 3K background up to the TeV energy range, is plotted toward the left for three different values of the magnetic field intensity. The regions used to estimate the SED in the TeV γ -ray and X-ray bands are different.

sar. However, the flux ratio $F(1-10 \text{ TeV})/F(2-10 \text{ keV})$ is unusually large compared with the typical PWNe; the ratios of Crab and RCW89 are 2.6×10^{-3} and 0.41 , respectively (Willingale et al. 2001; Aharonian et al. 2004; Aharonian et al. 2005c; DeLaney et al. 2006). In addition, the lack of radio emissions may be difficult to explain by assuming a PWN origin.

4.2. Src B

The best-fit value of the column density suggests that the distance to src B from us is similar to that to src A. There is an optical (Monet et al. 1999) and an infrared counterpart (Skrutskie et al. 2006), 2MASS J16140610-5152264, at $(l, b) = (331.^\circ 4579, -00.^\circ 5973)$, whose color also suggests extinction (Landi et al. 2006). Assuming a distance of 10 kpc, the luminosity of src B in the 2–10 keV band is $4 \times 10^{33} \text{ erg s}^{-1}$.

Src B was also detected with the Swift XRT (Landi et al. 2006). Their observed count rate was $(6.61 \pm 2.11) \times 10^{-3} \text{ c s}^{-1}$ in the 0.2–10 keV band. Landi et al. (2006) converted the count rate to the absorption-corrected flux of $5.4 \times 10^{-13} \text{ erg s}^{-1} \text{ cm}^{-2}$ in the 2–10 keV band by assuming a Galactic column density of $2 \times 10^{22} \text{ cm}^{-2}$ (Dickey & Lockman 1990) and a Crab-like spectrum. However, these parameters are not supported by our Suzaku results. We converted the count rate to the flux in the 2–10 keV band by assuming the best-fit parameters listed in table 2 with “WebPIMMS”⁷. The resulting observed flux was $(1.43 \pm 0.46) \times 10^{-13} \text{ erg s}^{-1} \text{ cm}^{-2}$. This suggests that time variability exists in src B, although the Suzaku flux of src B may have uncertainty, as described in section 3.2.

Since src B is in a relatively dim region in the TeV γ -

⁷ <http://heasarc.gsfc.nasa.gov/Tools/w3pimms.html>

ray band, this object seems hardly related to HESS J1614. However, if src A is the X-ray counterpart of HESS J1614, there still may be a remote possibility that src B may also be physically connected to HESS J1614, as suggested by the best-fit column density. One may speculate that HESS J1614 is an asymmetric PWN, such as MSH 15-52 (Aharonian et al. 2005c), and src B is a pulsar driving the nebula. The TeV γ -ray morphology suggests that HESS J1614 may consist of double-sided structures, and src B seems to reside between them (figure 1). The image of the TeV γ -ray emission from MSH 15-52 is also elongated and there is an indication that the TeV emission has peaks on both sides of pulsar PSR B1509–58. Pulsars within nebulae having a luminosity of 10^{33} erg s $^{-1}$ are not unusual. The spin down luminosity should be $\sim 10^{37}$ erg s $^{-1}$ (Cheng et al. 2004), then the TeV γ -ray emission of HESS J1614 can be driven by a few percent of the spin-down luminosity. The extremely large photon index of 3.6 is enigmatic, but consistent with the X-ray photon index of PSR J1809–1917 (Kargaltsev & Pavlov 2007b), which could conceivably associated with HESS J1809–193. However, at present, we observe no pulsation or radio emission from src B, as shown in figure 1.

4.3. Src C

The best-fit column density suggested that src C is a foreground source. From the SIMBAD Astronomical Database operated at CDS, Strasbourg, France⁸, we found a counterpart at $(l, b) = (331^\circ 58' 19'', -00^\circ 62' 51'')$ ⁹, which is a B9V star: HD 145703. The best-fit temperature and abundance are consistent with the X-ray observations of other late-type B stars (Stelzer et al. 2003).

4.4. Soft emission in the blank region

Within the bounds of our statistics, it is unclear whether the emission observed in the blank region is thermal or non-thermal. Given its soft and unabsorbed nature, this source may not be connected to HESS J1614 at all. Instead, we suspect that the emission is due to spatial fluctuation of the Galactic ridge emission, which is comprised of high (~ 7 keV) and low (~ 0.7 keV) temperature components (Kaneda et al. 1997). Since the best-fit column density is small, the soft excess emission may include the low temperature component. The best-fit temperature is between the high and low temperature components, and therefore the soft excess may also include high temperature component. We found no evidence suggesting the presence of soft emission in the hard band (0.5–2.0 keV) image of the ROSAT All-Sky X-ray Survey Broad Band data (RASS3bb, RASS-Cnt Broad).

5. Conclusions

The Suzaku results on the VHE γ -ray object HESS J1614–518 are summarized below.

1. Three X-ray objects, Suzaku J1614–5141 (src A), Suzaku J1614–5152 (src B), and Suzaku J1614–5148 (src C) are found in the Suzaku XIS field of view.
2. A hard extended source, src A, is the best candidate for the X-ray counterpart of HESS J1614–518.
3. Src A has a large flux ratio of $F(1–10 \text{ TeV})/F(2–10 \text{ keV}) \sim 34$ and a relatively small X-ray photon index of 1.7. It is difficult to explain these features by assuming that the TeV emission is due to the inverse-Compton scattering of the cosmic microwave background and that the X-rays are due to synchrotron radiation emitted by high-energy electrons.
4. The small photon index of src A can be explained in terms of non-thermal bremsstrahlung emission from the loss-flattened electron distribution.
5. Src B may not be physically related to HESS J1614–518. However, one remote possibility is a PWN scenario, in which src B is a pulsar driving the nebula.
6. Src C is a foreground B9V star, HD 145703.
7. We found a soft excess emission near HESS J1614–518, which is characterized either by a power-law with $\Gamma = 2.4$ or a thermal plasma with $kT = 2.7$ keV. This is probably not directly related to HESS J1614–518, but would nonetheless form a part of the Galactic ridge emission.

We are grateful to Profs. W. Hoffman and S. Funk for kindly providing us with the HESS image. We also thank all Suzaku members. We used the ROSAT Data Archive of the Max-Planck-Institut für extraterrestrische Physik (MPE) at Garching, Germany. This work is supported by the Grant-in-Aid for the 21st Century COE "Center for Diversity and Universality in Physics" from the Ministry of Education, Culture, Sports, Science and Technology (MEXT) of Japan. HM is also supported by the MEXT, Grant-in-Aid for Young Scientists (B), 18740105, 2007, and by The Sumitomo Foundation, Grant for Basic Science Research Projects, 071251, 2007. RY acknowledges support from the MEXT, Grant-in-Aid for Young Scientists (B), 18740153, 2007. KH thanks the support from the MEXT, Grant-in-Aid for Young Scientists (B), 19740143, 2007.

References

- Aharonian, F., et al. 2002, A&A, 393, L37
 Aharonian, F., et al. 2004, ApJ, 614, 897
 Aharonian, F., et al. 2005a, Science, 307, 1938
 Aharonian, F., et al. 2005b, A&A, 439, 1013
 Aharonian, F., et al. 2005c, A&A, 435, L17
 Aharonian, F., et al. 2006, ApJ, 636, 777
 Aharonian, F., et al. 2007, A&A, 467, 1075
 Anchordoqui, L. A., Beacom, J. F., Goldberg, H., Palomares-Ruiz, S., & Weiler, T. J. 2007, Phys. Rev. D, 75, 063001
 Anders, E. & Grevesse, N. 1989, Geochimica et Cosmochimica Acta, 53, 197

⁸ <http://simbad.u-strasbg.fr/simbad>

⁹ $(\alpha, \delta)_{J2000.0} = (16^{\text{h}} 14^{\text{m}} 48^{\text{s}}.5, -51^\circ 48' 31''.3)$

- Bamba, A., Yamazaki, R., Yoshida, T., Terasawa, T., & Koyama, K. 2005, *ApJ*, 621, 793
- Bamba, A., et al. 2007, *PASJ*, 59, S209
- Bock, D. C.-J., Large, M. I., & Sadler, E. M. 1999, *AJ*, 117, 1578
- Butt, Y. 2007, *astro-ph/0705.0189*
- Butt, Y. M., Drake, J., Benaglia, P., Combi, J. A., Dame, T., Miniati, F., & Romero, G. E. 2006, *ApJ*, 643, 238
- Cheng, K. S., Taam, R. E., & Wang, W. 2004, *ApJ*, 617, 480
- Cui, W., & Konopelko, A. 2006, *ApJL*, 652, L109
- DeLaney, T., Gaensler, B. M., Arons, J., & Pivovarov, M. J. 2006, *ApJ*, 640, 929
- Dickey, J. M., & Lockman, F. J. 1990, *ARA&A*, 28, 215
- Ebisawa, K., Maeda, Y., Kaneda, H., & Yamauchi, S. 2001, *Science*, 293, 1633
- Ebisawa, K., et al. 2005, *ApJ*, 635, 214
- Fleishman, G. D., & Bietenholz, M. F. 2007, *MNRAS*, 376, 625
- Horns, D., Hoffmann, A. I. D., Santangelo, A., Aharonian, F. A., & Rowell, G. P. 2007, *A&A*, in print (*astro-ph/0705.0009*)
- Ishisaki, Y., et al. 2007, *PASJ*, 59, S113
- Kaneda, H., Makishima, K., Yamauchi, S., Koyama, K., Matsuzaki, K., & Yamasaki, N. Y., 1997, *ApJ*, 491, 638
- Kargaltsev, O., Pavlov, G. G., & Garmire, G. P. 2007, *ApJ*, submitted (*astro-ph/0701069*)
- Kargaltsev, O., & Pavlov, G. G. 2007, *ApJ*, submitted (*astro-ph/0705237*)
- Kokubun, M., et al. 2007, *PASJ*, 59, S53
- Koyama, K., Makishima, K., Tanaka, Y., & Tsunemi, H., 1986, *PASJ*, 38, 121
- Koyama, K., et al. 2007, *PASJ*, 59, S23
- Landi, R., et al. 2006, *ApJ*, 651, 190
- Landi, R., de Rosa, A., Dean, A. J., Bassani, L., Ubertini, P., & Bird, A. J. 2007, *MNRAS*, 380, 926
- Matsumoto, H., et al. 2007, *PASJ*, 59, S199
- Mitsuda, K., et al. 2007, *PASJ*, 59, S1
- Monet, D. G., et al. 1999, *AJ*, 125, 984
- Morrison, R., & McCammon, D. 1983, *ApJ*, 270, 119
- Moskalenko, I. V., Porter, T. A., & Strong, A. W. 2006, *ApJL*, 640, L155
- Revnivtsev, M., Sazonov, S., Gilfanov, M., Churazov, E., & Sunyaev, R. 2006, *A&A*, 452, 169
- Serlemitsos, P. J., et al. 2007, *PASJ*, 59, S9
- Skrutskie, M. F., et al. 2006, *AJ*, 131, 1163
- Smith, R. K., Brickhouse, N. S., Liedahl, D. A., & Raymond, J. C. 2001, *ApJ*, 556, L91
- Stelzer, B., Huéramo, N., Hubrig, S., Zinnecker, H., & Micela, G. 2003, *A&A*, 407, 1067
- Sugizaki, M., Mitsuda, K., Kaneda, H., Matsuzaki, K., Yamauchi, S., & Koyama, K. 2001, *ApJS*, 134, 77
- Takahashi, T., et al. 2007, *PASJ*, 59, S35
- Tanaka, Y. 2002, *A&A*, 382, 1052
- Tawa, N., et al. 2007, *PASJ*, submitted
- Tian, W. W., Li, Z., Leahy, D. A., & Wang, Q. D. 2007, *ApJ*, 657, L25
- Torres, D. F., & Domingo-Santamaría, E. 2007, *Ap&SS*, 171
- Uchiyama, Y., Takahashi, T., Aharonian, F. A., & Mattox, J. R. 2002, *ApJ*, 571, 866
- Yamaguchi, H., et al. 2006, *Proc. SPIE*, 2006, 6266, 121
- Yamauchi, S., & Koyama, K. 1993, *ApJ*, 404, 620
- Yamazaki, R., Kohri, K., Bamba, A., Yoshida, T., Tsuribe, T., & Takahara, F. 2006, *MNRAS*, 371, 1975
- Warwick, R. S., Turner, M. J., L., Watson, M. G., & Willingale, R., *Nature*, 317, 218
- Willingale, R., Aschenbach, B., Griffiths, R. G., Sembay, S., Warwick, R. S., Becker, W., Abbey, A. F., & Bonnet-Bidaud, J.-M. 2001, *A&A*, 365, L212
- Worrall, D. M., Marshall, F. E., Boldt, E. A., & Swank, J. H. 1982, *ApJ*, 255, 111